Available online at www.sciencedirect.com
ScienceDirect
Ceramics International 35 (2009) 699–708
CERAMICS INTERNATIONAL
www.elsevier.com/locate/ceramint

Simulation of thermal and electric field evolution during spark plasma sintering

Devesh Tiwari [a], Bikramjit Basu [b,*], Koushik Biswas [c]

[a] Department of Computer Science and Engineering, Indian Institute of Technology Kanpur, India
[b] Department of Materials and Metallurgical Engineering, Indian Institute of Technology Kanpur, India
[c] Department of Metallurgical and Materials Engineering, Indian Institute of Technology Kharagpur, India

Received 11 October 2007; received in revised form 16 December 2007; accepted 4 February 2008
Available online 11 June 2008

Abstract

Finite element simulations have been conducted to determine the temperature distribution (both in radial and axial direction), heat and electric flux-field in the powder compact/die/punch assembly during the spark plasma sintering (SPS) process. A thermal–electrical coupled model with temperature dependent thermal and electrical properties is implemented. The simulation studies were conducted using both ABAQUS and MATLAB and a range of power input, varying thermal conductivity of powder compact were considered. Also, the effect of time variation on both thermal and electric field evolution was assessed. During SPS, the heat transmission pattern and the temperature difference between the specimen center and the die surface depend on thermal conductivity of the powder compact, time of sintering and power input. The simulation results also revealed that the temperature gradient across the powder compact/graphite die wall is higher for conditions of higher power input and/or powder compact with lower thermal conductivity.

Keywords: A. Sintering; A. Powders; C. Electrical conductivity

1. Introduction

The field assisted sintering technique (FAST) or pulsed electric current sintering (PECS), belongs to a class of novel sintering techniques that employs a pulsed direct current (DC) to enhance consolidation in order to produce sintered parts from metallic/ceramic powder [1]. In last one decade, various variants of FAST/PECS techniques, for example spark plasma sintering (SPS) [2], have been successfully used to consolidate a large variety of materials. A review on the historical background and recent research trends in sintering under electric field can be found elsewhere [2–10]. Until now, the SPS technology has been used to fabricate various materials including metals and alloys, compounds, ceramics, composites, especially some bulk amorphous and nanomaterials, multi scaled structure and functionally graded materials, etc. [11–15].

Although the mechanism of SPS process is still unclear to research community, nevertheless it surprisingly outperforms in many ways than various conventional sintering. This process ensures high thermo-efficiency, which is determined by the nature of heating in the SPS furnace and such heating phenomenon is fundamentally different from conventional sintering. In case of SPS, the pulsed DC current is made to pass through a graphite die–punch assembly, containing porous powder compact. In contrast, such die–punch assembly is heated by external heating source as in case of conventional sintering (hot pressing). During the process, the combination of a low voltage, high intensity pulsed direct current and uniaxial pressure is simultaneously applied, which in turn offers the possibilities of using rapid heating rates and very short holding times to obtain highly dense samples [16–18]. A strong electrical field is produced in the small gaps of the particles to make the electrons, cations and anions to strike the surface of the opposite particle and purify its surface. In parallel, SPS heating provides better self-purification of the surfaces, interfaces and grain boundaries. It is noteworthy to mention that a specific advantage of field assisted sintering, over traditional hot pressing or hot isostatic pressing, is controlled grain growth, which results into improved mechanical [19], physical [20] or optical properties [21].

* Corresponding author. Tel.: +91 512 2597771; fax: +91 512 2597505.
E-mail address: bikram@iitk.ac.in (B. Basu).

0272-8842/$34.00
doi:10.1016/j.ceramint.2008.02.013

The experiments carried out for electrically conductive [22–24] and non-conductive powders [24–26] demonstrated such attractive properties/property combination in the compacted materials. It has been believed that at initial stage, the pulsed DC current generates the spark discharge between the powder particles. The gases existing in the sample can be ionized and transformed into plasma. The generated spark discharges and plasma promote the elimination of absorbed gases and oxide layers on the surface of powder particles. Hence, the particle surfaces are cleaned and activated, which provides the favorable diffusion bonding between particles, thus accelerates the densification of the compact. Although, the claim that the pulses generate spark discharges and the existence of plasma between the powder particles explained the reason of the process being called as spark plasma sintering, the experimental evidences for the spark discharge and plasma are still lacking [11,12,27–31]. Moreover, the quantification of the effects of pulsed direct current on densification of the conducting powders has not been well-explored yet.

In summary, SPS process, to our understanding, is driven by three mechanisms (Fig. 1): (a) activation by pulsed current, (b) resistance sintering and (c) pressure application. The present research in the field of new materials is increasingly using the technology of SPS. The temperature field during sintering becomes an important consideration, because of the high heating-up involved in SPS. When sintering Ni powder using SPS [32], the temperature difference is above 130 °C from the center of the sample to the inner surface of die (highest temperature is 930 °C). Therefore, it is important to find out the temperature gradient distribution and the associated factors. Zavaliangos et al. [33] also reported the importance of the evaluation of temperature distributions during FAST. Their study enables a proper comparison between FAST and traditional sintering techniques and also indicates how to optimize processing parameters in larger size specimens. Hence, it is significant to study the special consolidation mechanisms of SPS process for sake of optimizing the processing parameters, as well as developing the potential applications of SPS technology.

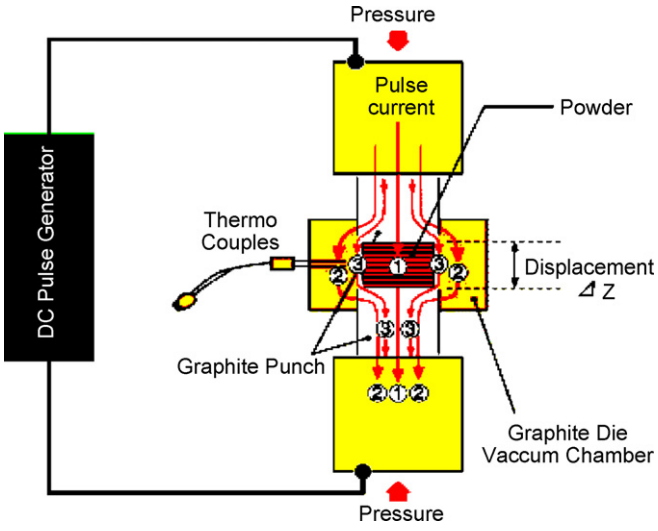

Fig. 1. Schematic of the physical process, involving the current flow during the spark plasma sintering process [5].

2. Current state of knowledge

The temperature field evolution during SPS has been investigated, by a few research groups. Yucheng and Zhengyi [34] calculated 2D temperature distribution inside the die, and their analysis confirms the temperature difference between the center and edge at the final stage of sintering in SPS system. It was further commented that higher is the thermal conductivity, lower is the temperature difference. Another conclusion of their work is that temperature difference is directly related to heating rate, i.e., higher the heating rate, greater is the temperature difference which can be as high as 450 K when sintering temperature at sample center is 1873 K. In a subsequent and more detailed study, Zavaliangos et al. [33] performed finite element simulation to study the similar problem of temperature distribution as well as its evolution during field activated sintering. Additionally, considerable temperature gradient, both in radial and axial direction, was analyzed in their work. They attempted to rationalize the finite element calculations from physical aspects of SPS, Joule's heat generation in the die set up and heat transfer within and out of die set up. Another important observation of their work is that almost linear co-relation exists between die surface temperature and the sample temperature.

Recently, similar FEM calculations have been performed by Van der Biest and coworkers [35] to model the evolution of current density and temperature distribution in SPS system. In order to validate the finite element model, some designed experiments were carried out on electrically conducting titanium nitride and electrically insulating zirconia powder compact. It has been concluded that a largely inhomogeneous temperature distribution can be expected to exist in case of titanium nitride when compared to zirconia sample under identical FAST cycles. Such difference can be attributed to difference in current flow in zirconia (current flow through punch and die) and titanium nitride (current flow through sample). Because of such a likely temperature distribution effect, a guideline to closely capture the temperature profile is proposed. It has been suggested that if a pyrometer is placed at bottom of bore hole inside the upper punch (about 5 mm away from specimen center), a better temperature control can be ensured with a temperature difference between the center and carefully placed pyrometer limited to 5 K or lower.

However, there has been limited attempt to study the densification mechanism during such a novel sintering route. In a recent attempt Song et al. investigated the phenomenon of neck growth during spark sintering of conducting metallic powder (copper) [15]. The influence of inhomogeneous temperature distribution on the microstructure development during the initial stages of spark plasma sintering has also been theoretically analyzed to quantify the effect of pulsed direct current. It was indicated that for conducting powder like copper, the intense joule heating effect at the particle conducting surface can often result in reaching the boiling point and therefore leads to localized vaporization or cleaning

of powder surfaces. Such phenomenon ensures favorable path for current flow. Additionally the neck growth behavior is experimentally observed to depend on the local distribution of current density. Importantly, they describe such growth that phenomenon follows self adjusting mechanism which leads to homogeneous distribution of neck sizes.

3. Model description

3.1. Temperature, heat and electrical flux distribution inside sample and die

3.1.1. ABAQUS formulation

Based on the schematic representation given in Fig. 2, and by exploiting symmetry of the setup, two-dimensional axisymmetric finite element models were developed for the thermal–electrical analyses. The finite element solutions were subsequently obtained using the ABAQUS explicit and implicit solvers [36,37].

The geometry, shown in Fig. 2, was used as a basis to conduct the thermal–electrical analysis. The apparent contact conditions, calculated for the different interfaces affect the electrical flow, heat generation and heat transfer. This model was solved using a fully coupled finite element formulation, which provides the electrical current density distribution, potential fields, heat generation and temperature history. To simulate the electric current flow through the setup, the magnitude of current was set as a pulsed current condition, while the potentials at the upper and lower graphite punch were set to +2.5 and −2.5 V.

To model current and heat flow across the interfaces, surface contact elements were applied to all the matching surfaces. The surface contact resistance was modeled using electrical contact conductance, ECC (Ω^{-1} m^{-2}) and thermal contact conductance, TCC (W^{-1} m^{-2} K^{-1}), which are both temperature and pressure dependent. The contact conductances are temperature dependent, because it is related to the conductivities of the contacting materials and to geometric changes of the gap due to applied load/pressure or relative thermal expansion. In the model, at each pair of contacting interface, the electrical current density, $\vec{J}$ (A m^{-2}) is calculated according to the following expression:

$$\vec{J} = \mathrm{ECC} \times (V_2 - V_1) \tag{1}$$

where $(V_2 - V_1)$ is the potential difference across the interfacial gap. Subsequently, the amount of heat flux, $\vec{q}$ (W/m^2) generated at the interface from the passage of electrical current (Joule heating) is given by

$$\vec{q} = \mathrm{TCC} \times (V_2 - V_1) \tag{2}$$

In the present model, only the temperature dependency was taken into account. The values of ECC and TCC were assumed to increase exponentially with temperature, following Eq. (3),

$$\mathrm{ECC}(T) \quad \text{or} \quad \mathrm{TCC}(T) = \frac{\beta \exp((T - T_0)/(T_\mathrm{L} - T_0))}{\alpha R_0 A_\mathrm{C}} \tag{3}$$

where R_0 is the static electrical (or thermal) contact resistance measured at reference temperature T_0, A_C is the contact area, α and β are empirical constants. Both ECC and TCC were assumed as infinite, if incipient fusion/melting occurs above the melting temperature, T_L.

3.1.2. MATLAB—a simple approach

In our study, the problem of temperature distribution in graphite die/punch/sample assembly is solved by assuming the heat transfer situation in case of axially symmetric cylinder [34].

The fundamental heat transfer equation to compute temperature $T(r,\theta, t)$ at any given radial distance 'r' and at any given time scale 't' is as follows:

$$\frac{1}{r}\frac{\partial}{\partial r}\left(r\frac{\partial T}{\partial r}\right) + \frac{\partial^2 T}{\partial \theta^2} + \dot{q} = \frac{1}{\alpha}\frac{\partial T}{\partial t} \tag{4}$$

where radial distance as r (m), temperature as T (K), time as t (s) and power input as $\dot{q}$ (W/m^3).

The solution of the Eq. (4) provides us the temperature gradient (steady state), as given in Eqs. (5) and (6):

$$\frac{\mathrm{d}T}{\mathrm{d}r} = -\frac{\dot{q}_1}{2k_1} \quad \text{when} \quad 0 \le r \le r_1 \tag{5}$$

$$\frac{\mathrm{d}T}{\mathrm{d}r} = -\frac{\dot{q}_2}{2k_2} - \frac{r_1^2(\dot{q}_1 - \dot{q}_2)}{2k_2}\frac{1}{r} \quad \text{when} \quad r_1 \le r \le r_2 \tag{6}$$

where sample radius as r_1 (m), die radius as r_2 (m), power input in sample as $\dot{q}_1$ (W/m^3), power input in die as $\dot{q}_2$ (W/m^3), thermal conductivity of sample as k_1 (W/(m K)), thermal conductivity of die as k_2 (W/(m K)), ambient temperature as T_∞ and surface temperature as T_2 (K).

The die surface temperature in steady state is governed by Eq. (7):

$$T_2 = \left\{\frac{1}{2\varepsilon\sigma}\left[\dot{q}_2 r_2 + \frac{r_1^2}{r_2^2}(\dot{q}_1 - \dot{q}_2) + T_\infty^4\right]\right\}^{1/4} \tag{7}$$

In the above equation, ε refers to the emissivity of the graphite and σ refers to Stefan–Boltzmann constant.

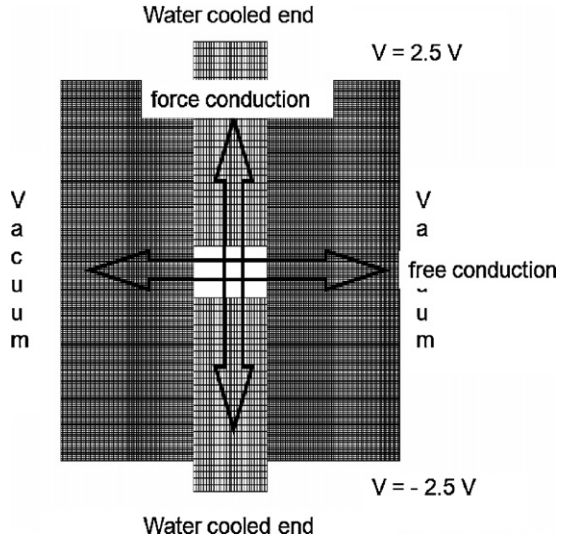

Fig. 2. The two-dimensional analysis of the thermal heat flow in the sample.

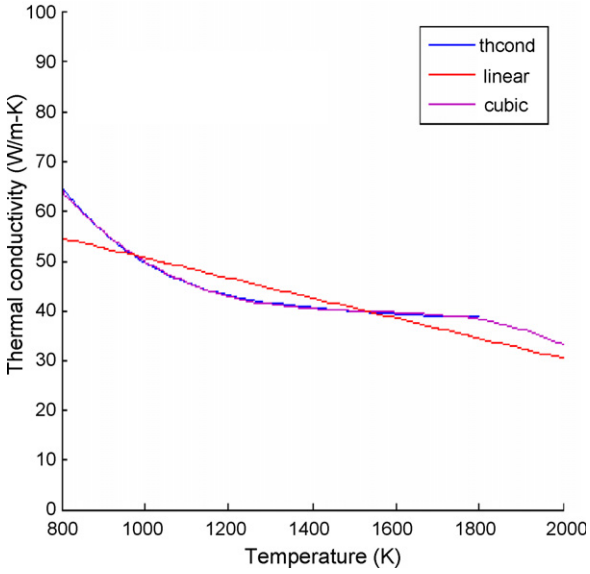

Fig. 3. Plot of thermal conductivity of graphite as a function of temperature. Note that the linear fit deviates from the thermal conductivity data, while the cubic fit overlaps with the thermal conductivity data.

We assume equal power input $(\dot{q}_1 = \dot{q}_2)$ and power input is evenly distributed in die and sample. The temperature dependence of thermal conductivity of graphite has been considered. In Fig. 3, the thermal conductivity of graphite is plotted against the temperature. On the same plot, the estimation using linear and cubic fit is also shown. While the linear fit noticeably deviates from the thermal conductivity variation, the cubic fit almost overlaps on the actual data, thereby indicating that the variation in thermal conductivity of graphite with temperature can be appropriately described by a cubic equation.

3.2. Surface temperature and electric field evolution in SPS system

We have considered the system with following dimensions:

Sample	Diameter	20 mm	Thickness	6 mm
Die	Diameter	46 mm	Height	40 mm
Punch	Diameter	20 mm	Length	30 mm
Base	Diameter	76 mm	Height	40 mm

We use graphite as material of die, sample and punch. We have considered the above dimensions of die and sample, so as to investigate how temperature and electric fields evolve during SPS process. It can be reiterated here that depending on electrical conductivity of the powder compact, a finite fraction of total current always passes through die wall. Therefore, the die wall thickness is important as it can clearly influence both the electric and thermal field evolution.

3.2.1. Simulation conditions

3.2.1.1. Material property. It is known that both thermal and electrical properties are temperature dependent. Fessler et al. [38] assumed the electrical properties to be constant resulting in decoupling of the problem. We are *coupling electrical and thermal problem*, and we believe that as described earlier this approach is better than that of Fessler et al. who first estimated the joule heating and then passed that value to heat transfer algorithms which results in *decoupling* of the problem. This approach is fundamentally different from what takes place in the real experiment.

3.2.1.2. Boundary condition. Following earlier reports by Groza and coworkers [33,39], we set extreme surface temperature at 320 K and the applied electrical voltage as 5 V. The application of DC current is assumed in the present case and it can be noted here that it has been reported that the pulsed current does not change the analytical results to a significant extent [40–42]. The interaction of die surface with external environment is taken care by considering the loss of heat by radiation with constant emissivity of 0.8. However, the heat loss through conduction and convection is neglected as the process is being carried out in vacuum. It needs to be recognized here that imperfect contact results into localized thermal and electrical resistance. The assumption of ideal surface, as also assumed by Anselmi-Tamburini and coworkers [40] and Anselmi-Tamburini et al. [41,42] is not appropriate in such a system. No assumption about the behavior of electrical or temperature field is considered in our work. In previous works, a part of the punch inside the die is being taken as integral part die; however we account them as separate entities.

3.2.1.3. Seeding and mesh generation. In our computational analysis, element size is set to be equal to 0.002, corresponding to approximately 34,000 nodes which are sufficiently high as it has been observed that shifting from 10,000 nodes to 35,000 nodes the results converge, while the color band representation goes to saturation at 15,000 nodes.

4. Results and discussion

4.1. Temperature distribution inside the sample and die

Following Eq. (7) and related assumptions of Section 3.1.2, the die surface temperature during SPS has been estimated

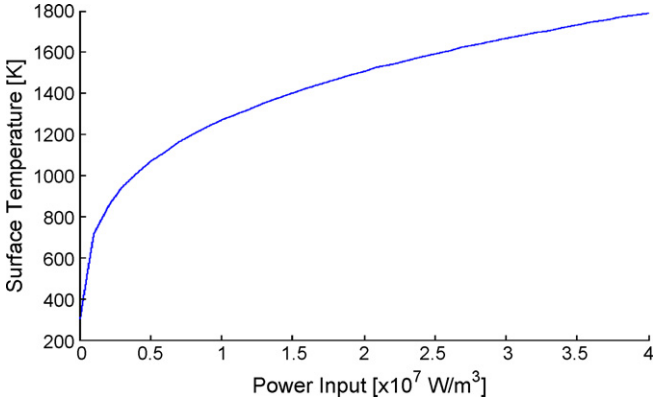

Fig. 4. The results of MATLAB estimation of graphite die surface temperature (as per Eq. (7), see Section 3.1.2) with variation in electrical power input. Note that the increase in surface temperature to more than 1000 °C is only feasible, when power input is more than 0.5×10^7 W/m^3.

using MATLAB. The surface temperature as a function of power input under steady state conditions is plotted in Fig. 4. Two characteristic features can be noted. Upto a power input of 0.5×10^7 W/m^3, the surface temperature steeply increases. When the power input exceeds 0.5×10^7 W/m^3, the die surface experiences higher temperature, i.e. more than 1000 °C. In the later regime, the temperature increase follows a near parabolic relationship. From Fig. 4, it is very clear that if SPS processing needs to be carried out at a temperature region corresponding to graphite die surface temperature of 1000 °C or higher, the

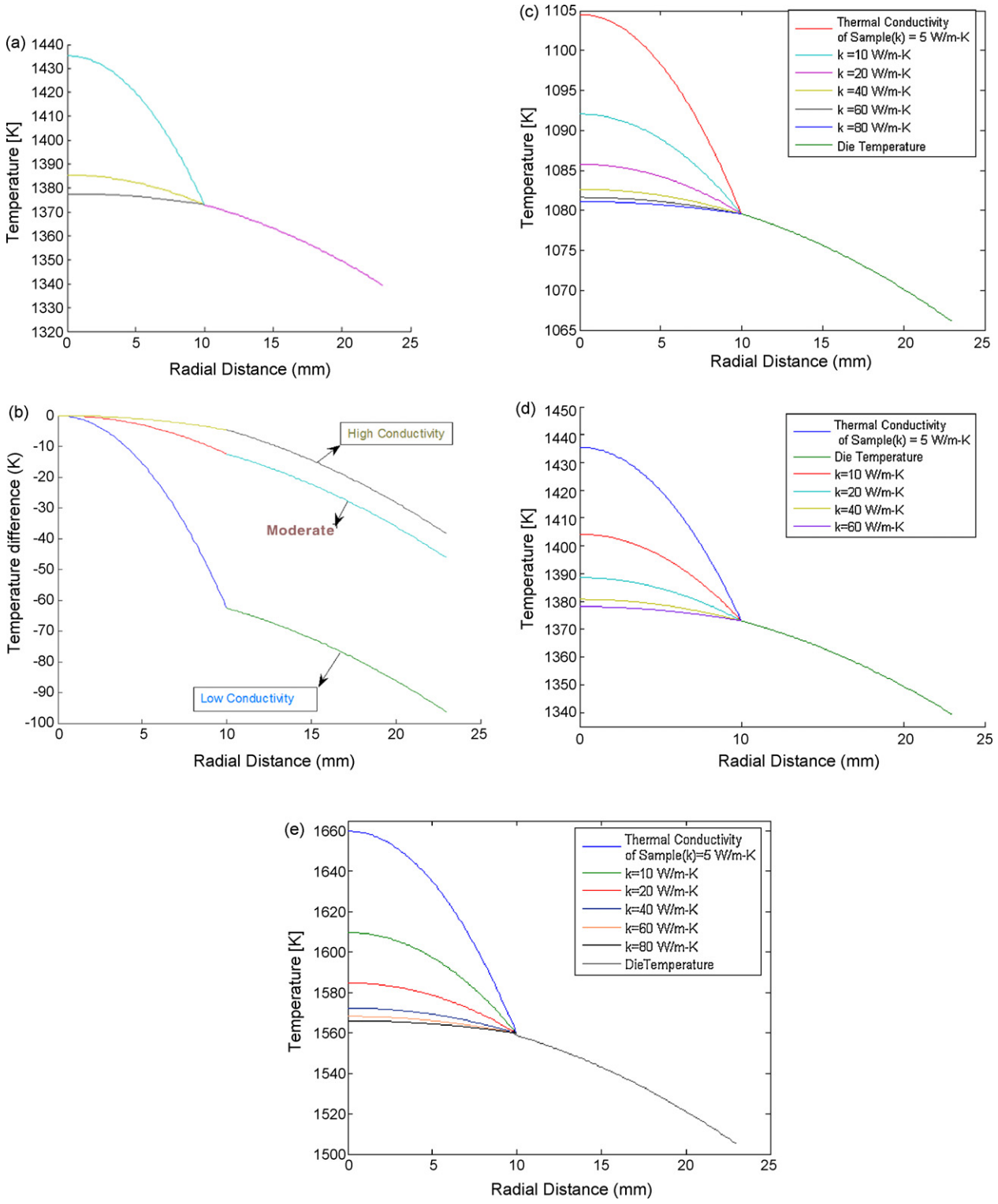

Fig. 5. The results of the MATALAB simulation depicting the thermal heat flow evolution in the powder compact/die system for various conditions: radial temperature profile in the middle cross-section of the sample at a constant Joule heat density (1.25×10^7 W/m^3) (a and b) and the effect of temperature independent heat conductivity on the temperature profile at Joule heat density of 0.5×10^7 W/m^3 (c), 1.25×10^7 W/m^3 (d) and 2.0×10^7 W/m^3 (e).

electrical power supply enabling power input to the SPS system to more than 0.5×10^7 W/m^3 needs to be used.

An increase in die surface temperature from 1000 to 1700 K can be realized with seven times increase in power input, i.e., from 0.5×10^7 to 3.5×10^7 W/m^3. Following this we have investigated the temperature distribution in the die/sample system. For Fig. 5(a) and (b), the power input has been set to 1.25×10^7 W/m^3, which is also used for our ABAQUS experiments. ABAQUS approach has been discussed in great detail in further sections. Three different relative values of the thermal conductivity of the sample are assumed for Fig. 5(a) and (b). We have used Eqs. (4)–(6) to obtain quantitative predictions of temperature as a function of radial distance from the center of cylindrical die. From the data plotted in Fig. 5(b) the temperature decreases with increase in radial distance, irrespective of thermal conductivity. However, such a decrease strongly depends on the relative difference in thermal conductivity of various powder samples. For example if we consider the use of a 46 mm diameter die, the temperature difference between center and the edge is around 50 K for high (66 W/(m K)) and moderate (40 W/(m K)) thermal conductivity. However, a temperature difference of 100 K can be observed for material with low conductivity (5 W/(m K)). Another important aspect, which can be inferred from Fig. 5(b), is that larger the diameter more is the temperature difference between center and edge of die. For a 46 mm diameter die, the temperature difference of 90 K for low thermal conductivity sample and around 25–35 K for moderate/high thermal conductivity material can be expected.

Next, we analyze the effect of power input on temperature distribution inside sample and die. Three different power inputs (0.50×10^7, 1.25×10^7, 2.00×10^7 W/m^3) have been used in our work. Fig. 5(c)–(e) depict variation of temperature as function of thermal conductivity for different level of power input. Careful observations lead to few important implications. For low power input, the drop in temperature from center to edge is low. Higher power input produces more than three times of temperature drop as compared to low power input. Clearly, the center of the die attains higher temperature in steady state for higher level of power input. Quantitatively, with power input of 0.50×10^7 W/m^3, the die center achieves a temperature of 1100 K; however increasing power input to 2.00×10^7 W/m^3 produces temperature of around 1650 K at the center. It should be noted that in both cases, material of same thermal conductivity (5 W/(m K)) has been used. Further we observe the effect of thermal conductivity with respect to the power input. For a given power input, we note different temperature drop, with change in thermal conductivity. This temperature drop is high for low thermal conductivity materials, but as we increase thermal conductivity of sample, fall in temperature from center towards end of sample dies down. It is almost negligible for thermal conductivity equal to or higher than 80 W/(m K). On the other hand, low thermal conductivity materials assist in producing large temperature gradient. For instance, at power input of 1.25×10^7 W/m^3 a low conductivity material experiences a temperature fall of around 60 K in temperature from center to edge of the sample. Such phenomenon is well assisted by physics of conduction. A low thermal conductive material allows heat to flow with less resistance and hence a significant drop in temperature is observed as we move away from center of sample. This should be noted that the rate of fall in temperature across graphite die is same for all power input values, because it solely depends on thermal conductance of graphite. However, actual numerical values of temperature across die are different as we change power input level. Higher power input produces higher values of temperature, as discussed earlier too.

4.2. Surface temperature and electric field evolution in SPS system

The simulation results, obtained using ABAQUS software are presented below in terms of three important aspects:

(a) Temperature field.
(b) Electric field (electric current density).
(c) Heat flux.

In selected cases, the ABAQUS results were compared with complementary analysis, carried out using MATLAB. In our

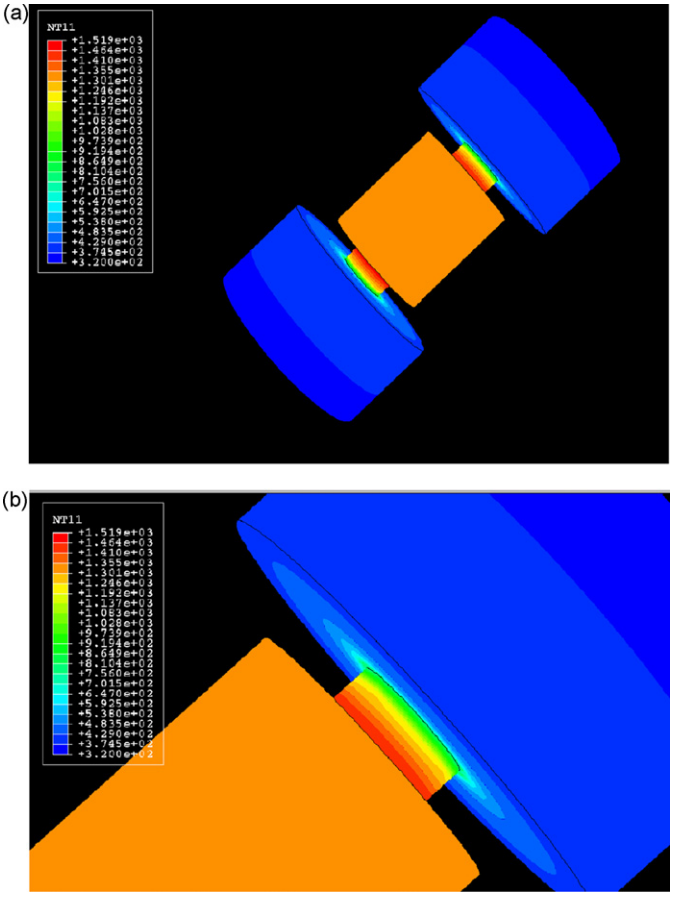

Fig. 6. ABAQUS FEM simulations visualizing the temperature distribution on the die and punch surface after 450 s operation of spark plasma sintering at a constant Joule heat density of 1.25×10^7 W/m^3: (a) overall view of the entire system of graphite plate/punch/die system and (b) closer view of the region of top punch and graphite punch/graphite plate interface.

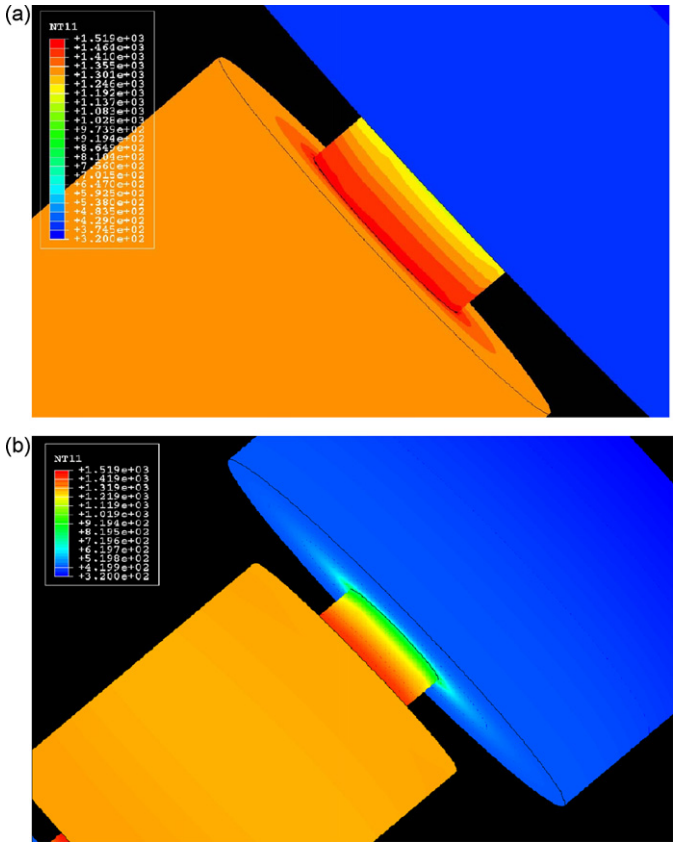

Fig. 7. ABAQUS FEM simulations visualizing the temperature distribution on the die and punch surface after 450 s operation of spark plasma sintering at a constant Joule heat density of 1.25×10^7 W/m^3: (a) closer view of the graphite die surface and (b) closer view of the region of punch and graphite punch/graphite plate interface.

ABAUS simulation, a constant power input of 1.25×10^7 W/m^3 has been considered.

4.2.1. Temperature field

The evolution of temperature field over the system is simulated after two representative situations of 450 and 90 s, during the spark plasma sintering experiments. After 450 s (refer Figs. 6 and 7) the surface temperature is in the range of 1301–1355 K (average ~1325 K) which is slightly lower (~14–15°) than obtained by MATLAB analysis (value ~1339 K). It can be further mentioned here that Munir's group performed similar simulation (450 s) and obtained a die surface temperature of 1273 K whereas their experimentally finding was 1323 K [40–42]. This result was very close to our model predicted temperature of 1325 K.

Although there are some difference in results obtained for longer sintering time, the temperature, heat and current flux distribution after 90 s (Fig. 8) have good correlation with our simulation results as well as with that of the earlier reported results by Anselmi-Tamburini and coworkers [40] and Anselmi-Tamburini et al. [41,42]. It can be noted here that Munir's group also neglected the heat transfer (conduction radiation) and they calculated the temperature increase due to Joule heating, which is proportional to the corresponding

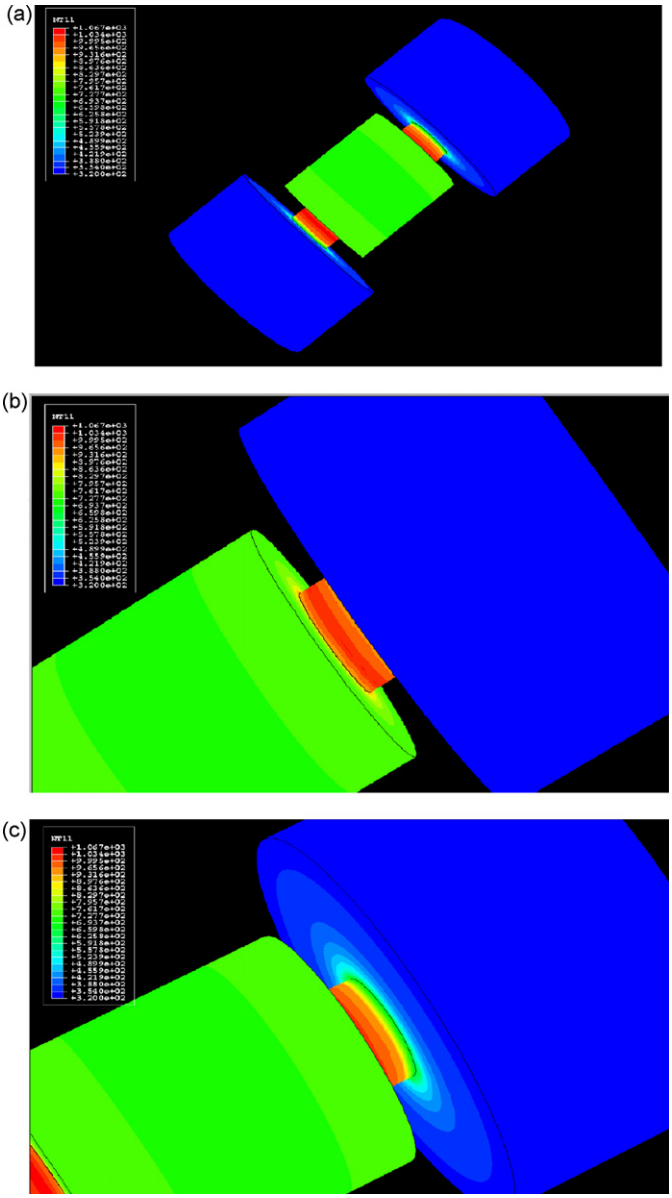

Fig. 8. ABAQUS FEM simulations visualizing the temperature distribution on the die and punch surface at a constant Joule heat density of 1.25×10^7 W/m^3 after 90 s of during spark plasma sintering experiment: (a) entire system of graphite plate/punch/die system; (b and c) closer view of the temperature profile at the region of punch and at graphite punch/graphite plate interface.

resistance in the system. However, the heat transfer situation modifies the initial temperature distribution.

From our simulation results, it can be commented that the highest temperature in the system develops in the punches during the early stages. The generated heat is partially diffused into the specimen and partially lost into the machine (upper and lower graphite spacers), which is water cooled (a force conduction situation). As the process progresses, the temperature in the specimen increases due to thermal conduction from the punches. In addition, the surface radiation causes a secondary heat loss for the specimen/die assembly. This pattern of heat flow results in a temperature differential between die surface and specimen center with the specimen center at a higher temperature than the control temperature on the surface of the die.

Additionally, the temperature gradients should be realized while carefully noting higher temperature in punches. Full punch should not be expected to be at higher temperature than other parts. Arguing that a part near to sink to be at highest temperature does not sound reasonable too. The larger magnified simulation results (Fig. 8c) enable us to explore the effect of contact resistance and radial temperature gradient.

4.2.2. Electric field

As far as the simulated distribution of electric current density (ECD) is concerned, Fig. 9 shows clear difference in ECD between graphite punch and die surface. In particular, the electric current is maximum at the part of the punch outside the die, due to smallest cross-section area (see red region/band). Although the magnitude of the current varies during sintering, the pattern of current flow is practically independent of time for the specific simulated application. Again the punches experience mostly high ECD and therefore Joule's heating is in accordance with ECD. We can comment that Joule's heating dominates in the punch part, as it should be. Overall, our ABAQUS simulation results reveal lowest ECD on die surface, while intermediate level ECD at the punch area.

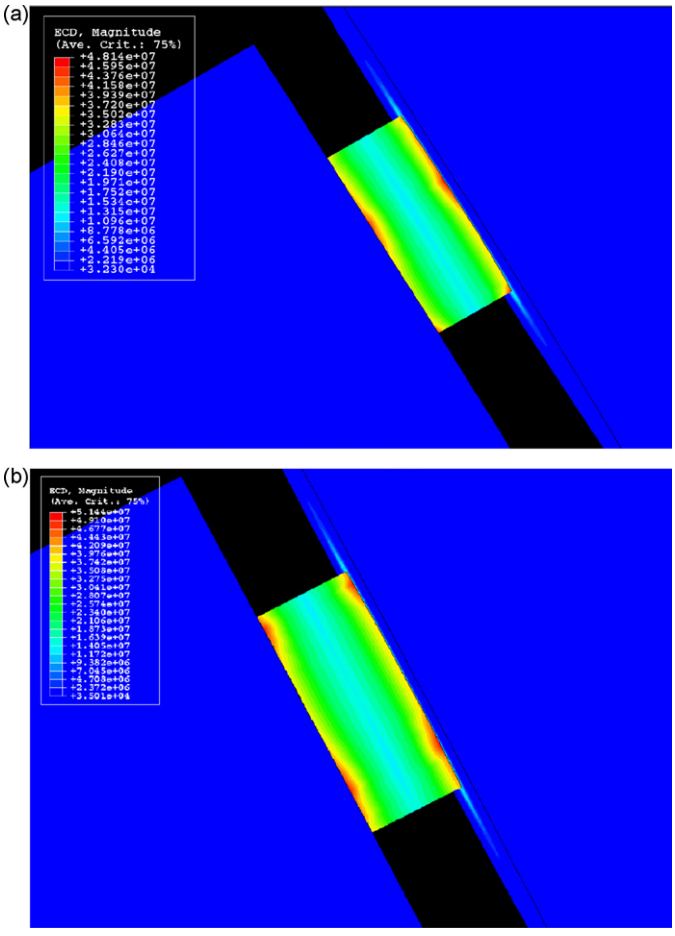

Fig. 9. ABAQUS FEM simulations visualizing the temperature distribution on the die and punch surface of spark plasma sintering at a constant Joule heat density of 1.25×10^7 W/m^3 for various conditions: (a) after 450 s of soaking and (b) after 90 s of soaking during spark plasma sintering experiments.

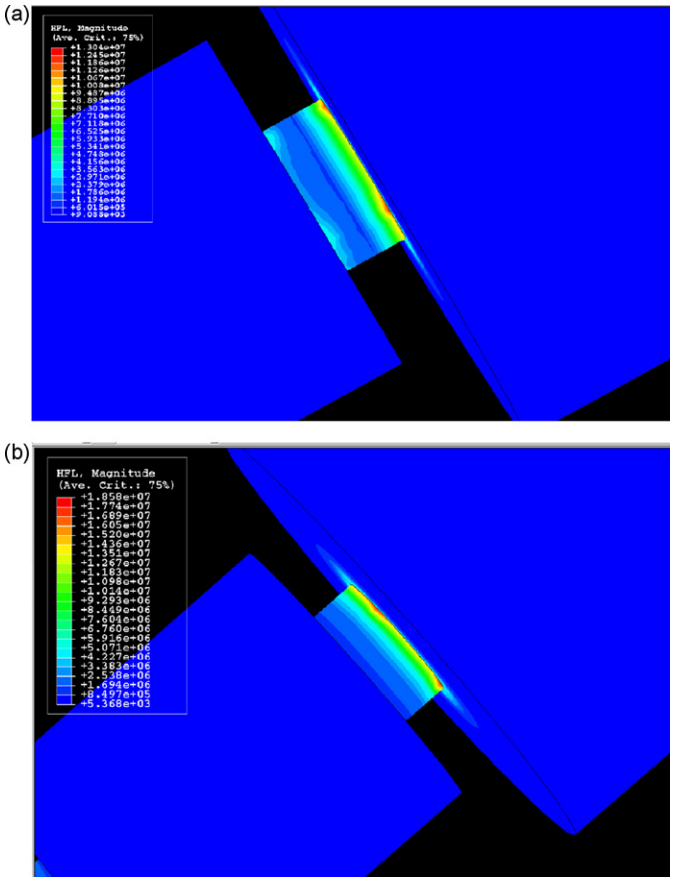

Fig. 10. ABAQUS FEM simulations visualizing the temperature distribution on the die and punch surface at a constant Joule heat density of 1.25×10^7 W/m^3: (a) after 90 s of soaking and (b) after 450 s of soaking during spark plasma sintering experiments.

Our results again are not valid only on physical basis, but also agree with the work by Gorza and coworkers [33,39]. As stated earlier, ECD trend does not change over the time, however the numerical values differ. This can be confirmed from snapshots taken after 90 s of simulation (Fig. 9c).

4.2.3. Heat flux

The simulation results of the heat flux evolution over same two events have been presented in Fig. 10. Since the punches are at higher temperature with less surface area, the existence of a clear gradient can be seen in the punches for two simulated events. For example, after simulation experiment of 90 s, the interface of die/punch shows more non-uniform heat flux distribution compared to that after little more holding time of 450 s. In both cases, the upper interface of punch with top ram experiences more heat flux (indicated by red region). It is possible that such gradient in heat flux can result in inhomogeneous heat generation for the die/sample assembly.

5. Conclusions

A fully coupled thermo-electrical finite element analysis using ABAQUS and MATLAB was conducted for varying thermal conductivity powder compacts and for condition of

different power input with an aim to understand some aspect of spark plasma sintering and following major points emerge from our study:

(a) The temperature profile across powder compact is strongly sensitive to both power input and thermal conductivity. Irrespective of power input level, no significant difference in the temperature gradient is observed for thermal conductivity value of 40 W/(m K) or above. For powder compact of lower thermal conductivity (20 W/(m K) or lower), the difference in maximum temperature, attained at sample center increases with increasing power input level.
(b) Our simulation results (ABAQUS) reveal that maximum surface temperature is attained at the punch region, closer to the die/punch interface at steady state conditions (450 s). The graphite plate remains at the room temperature.
(c) At the transient conditions (90 s) the die surface temperature is found to be at much lower temperature, when much higher temperature is reached at the graphite punch region.
(d) As far as evolution in electric current density is concerned, the maximum level is attained at the central part of the graphite punch/die interfacial region at steady state condition (450 s); however the maximum current density is more spread at the two end regions of graphite punch/die interfacial area. Also the simulation results indicate that rather uniform heat flux condition can be realized during steady state at die/punch interfacial area and deviation from uniformity can be observed towards the graphite punch/graphite plate (top/bottom electrode) contact region.

Acknowledgments

Devesh wishes to extend his thanks to Dr DY Kim and Dr N M Hwang for useful discussions during short stay at Seoul National University, South Korea in the summer 2005. Devesh would also like to thank the group members of Sintering and Microstructure lab, Creative Research Centre, School of Materials Research Centre, School of Material Science, and SNU, South Korea.

References

[1] J.R. Groza, Field assisted sintering, ASM Handbook, Powder Metall. 7 (1998) 583–589.
[2] O. Yanagisawa, T. Hatayama, K. Matsugi, Recent research on spark sintering, Mater. Jpn. (Japan) 33 (12) (1994) 1489–1496.
[3] J.R. Groza, A. Zavaliangos, Sintering activation by external electrical field, Mater. Sci. Eng. A 287 (2) (2000) 171–177.
[4] G.D. Cremer, Sintering Together Powders Metals such as Bronze, Brass or Aluminum, US Patent No. 2,355,954 (August 1944).
[5] A. Mukhopadhyay, B. Basu, Consolidation–microstructure–property relationships in bulk nanoceramics and ceramic nanocomposites: a review, Int. Mater. Rev. 52 (5) (2007) 257–288.
[6] B. Basu, T. Venkateswaran, D.-Y. Kim, Microstructure and properties of spark plasma sintered ZrO_2–ZrB_2 nanoceramic composites, J. Am. Ceram. Soc. 89 (8) (2006) 2405–2412.
[7] B. Basu, J.-H. Lee, D.-Y. Kim, Development of nanocrystalline wear resistant Y-TZP ceramics, J. Am. Ceram. Soc. 87 (9) (2004) 1771–1774.
[8] B. Basu, J.-H. Lee, D.-Y. Kim, Development of WC–ZrO_2 nanocomposites by spark plasma sintering, J. Am. Ceram. Soc. 87 (2) (2004) 317–319.
[9] T. Venkateswaran, B. Basu, G.B. Raju, D.-Y. Kim, Densification and properties of transition metal borides-based cermets via spark plasma sintering, J. Eur. Ceram. Soc. 26 (2006) 2431–2440.
[10] T. Venkateswaran, D. Sarkar, B. Basu, Tribological properties of WC–ZrO_2 nanocomposites, J. Am. Ceram. Soc. 88 (3) (2005) 691–697.
[11] R.S. Dobedoe, G.D. Wost, M.H. Lewis, Spark plasma sintering of ceramics, Bull. Eur. Ceram. Soc. 1 (2003) 19–24.
[12] C. Shearwood, Y.Q. Fu, L. Yu, K.A. Khor, Spark plasma sintering of TiNi nano-powder, Scripta Mater. 52 (6) (2005) 455–460.
[13] Y.H. Kim, J.H. Kang, J.S. Kim, Spark-plasma sintering of oxidized spherical Fe-powder, in: Proceedings of NEDO International Symposium on Functionally Graded Materials, Kyoto, Japan, (1999), pp. 123–126.
[14] J. Schmidt, W. Schnelle, Y. Grin, R. Kniep, Pulse plasma synthesis and chemical bonding in magnesium diboride, Solid State Sci. 5 (2003) 535–539.
[15] X. Song, X. Liu, J. Zhang, Neck formation and self-adjusting mechanism of neck growth of conducting powders in spark plasma sintering, J. Am. Ceram. Soc. 89 (2) (2006) 494–500.
[16] M. Tokita, Mechanism of spark plasma sintering, in: K. Kosuge, H. Nagai (Eds.), Proceedings of the 2000 Powder Metallurgy World Congress, Kyoto, Japan, November 2000, Japanese Society of Powder and Powder Metallurgy, Kyoto, Japan, 2001, pp. 729–732.
[17] V. Mamedov, Spark plasma sintering as advanced PM sintering method, Powder Metall. 45 (4) (2002) 322–328.
[18] Z.J. Shen, M. Johnson, Z. Zhao, M. Nygren, Spark plasma sintering of alumina, J. Am. Ceram. Soc. 85 (8) (2002) 1921–1927.
[19] Z. Shen, Z. Zhao, H. Peng, M. Nygren, Formation of tough interlocking microstructures in silicon nitride ceramics by dynamic ripening, Nature 417 (2002) 266–269.
[20] K.A. Khor, K.H. Cheng, L.G. Yu, F. Boey, Thermal conductivity and dielectric constant of spark plasma sintered aluminium nitride, Mater. Sci. Eng. A 347 (2003) 300–305.
[21] X. Su, P. Wang, W. Chen, Z. Shen, M. Nygren, C. Yibing, et al., Effects of composition and thermal treatment on infrared transmission of Dy-α-sialon, J. Eur. Ceram. Soc. 24 (2004) 2869–2877.
[22] S.W. Wang, L.D. Chen, T. Hirai, Effect of plasma activated sintering (PAS) parameters on densification of copper powder, Mater. Res. Bull. 35 (4) (2000) 619–628.
[23] H.T. Kim, M. Kawahara, M. Tokita, Specimen temperature and sinterability of Ni powder by spark plasma sintering, J. Jpn. Soc. Powder Powder Metall. (Japan) 47 (8) (2000) 887–891.
[24] L.A. Stanciu, V.Y. Kodash, J.R. Groza, Effects of heating rate on densification and grain growth during field-assisted sintering of α-Al_2O_3 and $MoSi_2$ powders, Metall. Mater. Trans. A 32A (10) (2001) 2633–2638.
[25] M. Omori, Sintering, consolidation, reaction and crystal growth by the spark plasma system (SPS), Mater. Sci. Eng. A 287 (2) (2000) 183–188.
[26] S.W. Wang, L.D. Chen, T. Hirai, Densification of Al_2O_3 powder using spark plasma sintering, J. Mater. Res. 15 (4) (2000) 982–987.
[27] J.-M. Lee, S.-B. Kang, T. Sato, H. Tezuka, A. Kamio, Fabrication of Al/Al_3Fe composites by plasma synthesis method, Mater. Sci. Eng. A343 (2003) 199–209.
[28] M. Tokita, Large-size WC/Co functionally graded materials fabricated by spark plasma sintering (SPS) method, in: Proceedings of the Seventh International Symposium on Functionally Graded Materials, FGM 2002, Beijing, China, (2002), pp. 1–8.
[29] J.D. Hansen, R.P. Rusin, M.H. Teng, D.L. Johnson, Combined-stage sintering model, J. Am. Ceram. Soc. 75 (5) (1992) 1129–1135.
[30] M. Omori, Sintering, consolidation, reaction and crystal growth by the spark plasma system (SPS), Mater. Sci. Eng. A287 (2000) 183–188.
[31] S.W. Wang, L.D. Chen, T. Hirai, Y.S. Kang, Microstructure inhomogeneity in Al_2O_3 sintered bodies formed during the plasma-activated sintering process, J. Mater. Sci. Lett. 14 (7) (1999) 1119–1121.
[32] K. Hwan-tae, K. Masakazu, T. Masao, J. Jpn. Soc. Powder Metall. 47 (8) (2000) 887–891.

[33] A. Zavaliangos, J. Zhang, M. Krammer, J.R. Groza, Temperature evolution during field activated sintering, Mater. Sci. Eng. A 379 (2004) 218–228.
[34] W. Yucheng, F. Zhengyi, Study of temperature field in spark plasma sintering, Mater. Sci. Eng. B 90 (1–2) (2002) 34–37.
[35] K. Vanmeensel, A. Laptev, O. Van der Biest, J. Vleugels, Field assisted sintering of electro-conductive ZrO_2-based composites, J. Eur. Ceram. Soc. 27 (2–3) (2007) 979–985.
[36] ABAQUS, ABAQUS/Standard User's Manuals, Version 6.3, Hibbitt, Karlsson & Sorensen, Inc., USA, 2003.
[37] ABAQUS, ABAQUS/Explicit User's Manuals, Version 6.3, Hibbitt, Karlsson & Sorensen, Inc., USA, 2003.
[38] R.F. Fessler, F.C. Chang, B.D. Merkle, J.M. Borton, W.M. Goldberger, Modeling the Electroconsolidation® Process, in: Proceedings of the International Conference on Powder Metallurgy and Particulate Materials, New York, NY, 2000.
[39] J. Zhang, A. Zavaliangos, J.R. Groza, A model for simulation of temperature field evolution in field activated sintering, in: Proceedings of the Sintering, vol. 9, Penn State, (2003), pp. 14–17.
[40] W. Chen, U. Anselmi-Tamburini, J.E. Garay, J.R. Groza, Z.A. Munir, Fundamental investigations on the spark plasma sintering/synthesis process. I. Effect of dc pulsing on reactivity, Mater. Sci. Eng. A 394 (1–2) (2005) 132–138.
[41] U. Anselmi-Tamburini, S. Gennari, J.E. Garay, Z.A. Munir, Fundamental investigations on the spark plasma sintering/synthesis process. II. Modeling of current and temperature distributions, Mater. Sci. Eng. A 394 (1–2) (2005) 139–148.
[42] U. Anselmi-Tamburini, J.E. Garay, Z.A. Munir, Fundamental investigations on the spark plasma sintering/synthesis process. III. Current effect on reactivity, Mater. Sci. Eng. A 394 (1–2) (2005) 139–148.